Free-Space Laser Communication and Active Laser Illumination III, edited by David Voelz, Jennifer C. Ricklin, Proceedings of SPIE Vol. 5160, San Diego, CA, August 4 - 6, 2003.

Comparison of Macro-Tip/Tilt and Meso-Scale Position Beam-Steering Transducers for Free-Space Optical Communications Using a Quadrant Photodiode Sensor

K.B. Fielhauer*[a], B.G. Boone**[a], J.R. Bruzzi[a], B.E. Kluga[a], J.R. Connelly[a], M.M. Bierbaum[a]
and
J.J. Gorman[b], N. Dagalakis[b]

[a] Johns Hopkins University Applied Physics Laboratory, Space Department,
11100 Johns Hopkins Rd., Laurel, MD 20723-6099
[b] National Institute of Standards and Technology, Manufacturing Engineering Laboratory,
100 Bureau Dr., Stop 8230, Gaithersburg, 20899-2830

ABSTRACT

The National Aeronautics and Space Administration (NASA) plans to develop optical communication terminals for future spacecraft, especially in support of high data rate science missions and manned exploration of Mars. Future, very long-range missions, such as the Realistic Interstellar Explorer (RISE)[1], will need optical downlink communications to enable even very low data rates. For all of these applications, very fine pointing and tracking is also required, with accuracies on the order of ± 1 μrad or less and peak-to-peak ranges of ± 10 mrad or more. For these applications, it will also be necessary to implement very compact, lightweight and low-power precision beam-steering technologies. Although current commercial-off-the-shelf devices, such as macro-scale piezo-driven tip/tilt actuators exist, which approach mission requirements, they are too large, heavy, and power consuming for projected spacecraft mass and power budgets. The Johns Hopkins University Applied Physics Laboratory (JHU/APL) has adopted a different approach to beam-steering in collaboration with the National Institute of Standards and Technology (NIST). We are testing and planning to eventually package a highly accurate large dynamic range meso-scale position transducer under development at NIST. In this paper we will describe a generic package design of an optical communications terminal incorporating the NIST prototype beam-steerer. We will also show test results comparing the performance of the NIST prototype meso-scale position beam-steerer to a commercial macro-tip/tilt actuator using a quad-cell tracking sensor.
Key words: beam-steering, quadrant photodetector, tip/tilt, position transducer, optical communications

1. INTRODUCTION AND BACKGROUND

1.1 System applications and requirements

The Johns Hopkins University Applied Physics Laboratory is developing optical communications system architectures by initially using state-of-the-art commercial off-the-shelf components and then replacing them with more advanced technology components as they become available for insertion into our architectures at lower risk. The range of applications include: deep space (represented by our civilian-space business area) and near terrestrial space (represented by our military-space business area). Deep space applications include live video from Mars as well as eventually interstellar probe downlinks[1]. These applications entail a single dedicated channel having a very high pointing accuracy (~300-400 nrad) but only modest bandwidth (~10-100 MHz, depending on range) relative to terrestrial optical telecom bandwidths. Near terrestrial space applications are essentially represented by geosynchronous earth orbit (GEO) to ground optical links, which in the near term are principally intended for military applications. In these applications the links may be multi-channel, require high accuracy pointing (~5-10 μrad), and entail very high bandwidths (~10 GHz). Thus the desired data rates and pointing accuracy requirements are driven by two distinct environments differing primarily in link range. Of course, link margin decreases with range, but laser source power and receiver sensitivity constrain the achievable data rate for a desired bit error rate.

*Karl.Fielhauer@jhuapl.edu; phone 443-778-3147; **Brad.Boone@jhuapl.edu; phone 443-778-6778

Optimal pointing error is about one third of the beamwidth for a single-mode diffraction-limited Gaussian beam. This follows from trading-off two terms in the link equation: antenna gain and pointing loss, assuming a Gaussian beam profile. From typical spacecraft platform vibration spectra,[2] as exemplified by the empirical data shown in Figure 1, we can infer that a reasonable 3σ requirement for fine tracking and stabilization for most deep space missions (Mars and beyond) must approach the 1 μrad level over a bandwidth approaching 200-400 Hz. Additional requirements for testing the pointing and tracking control loop drive us to adopt some simple criteria for servo control in the form of a proportional-integral (PI) control system having an open-loop minimum gain margin of 6 dB and minimum phase margin of 0.7 rad. Finally, we also must demonstrate that we can achieve the tracking requirements at the same time as we are communicating, that is, we must not only achieve the tracking requirements following acquisition (when the laser beam could be from a beacon in a higher power mode), but also during communications when we must maintain the track loop under an average power that would vary with the communications modulation duty cycle. Of course, there are also situations in deep space where it doesn't make sense to use beacon tracking at all, because the loop delay is too long. In that case we must maintain track using either the earth as a beacon or operate the attitude control and pointing system entirely open-loop via a star tracking mechanism augmented with an inertial measurement unit, earth ephemeris update, accurate on-board clock, and Kalman filter. This has been described elsewhere[3].

This latter approach, although the most essential and desirable from an operational point of view in deep space, is not the focus of this paper. We are interested in measuring and comparing the performance of different beam-steering technologies for deep space or near terrestrial space using simply a quadrant photodiode sensor, although we are also investigating the use of focal plane arrays for measuring performance and supporting pointing and tracking.

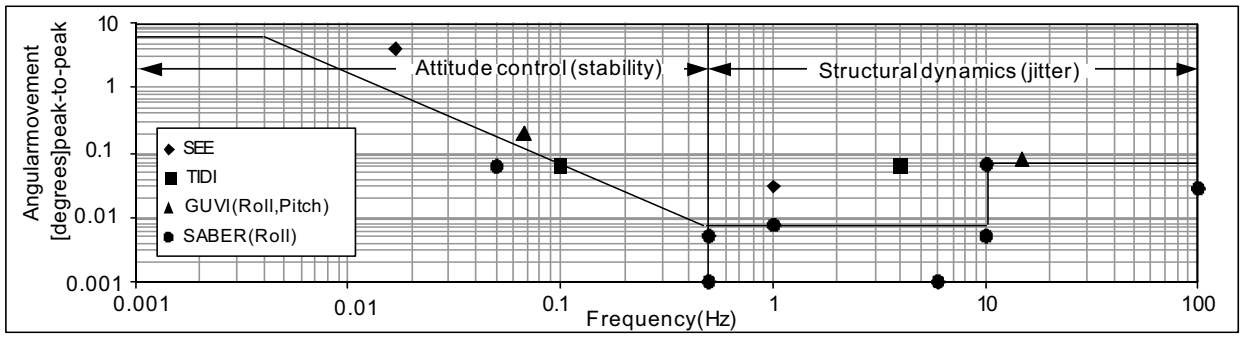

Figure 1: Vibration spectra for typical spacecraft and spacecraft instruments showing most energy is confined to frequencies below 100 Hz (although some local mechanical resonances may be higher, but still less than 1000 Hz).

Two near-term alternative beam-steering technologies that we have focused on are both electro-mechanical. They offer adequate bandwidth, are lower risk, and are more optically efficient than (otherwise attractive technologies such as) liquid crystal, photorefractive or quantum well device technologies, which are still in development. These two devices are macro–tip/tilt, and macro- and meso-scale[4] two degree-of-freedom position transducers. The two key tracking sensors that we are evaluating and developing are: quadrant photodiode detectors, and CCD FPA star trackers. We will focus on the quad detector in this paper. We have already developed a modulator/demodulator approach for modest bandwidth optical transceivers suitable for deep space[5]. In this paper, however, we will describe tests and results using simply an un-modulated CW laser beam of sufficient power to determine the lower bound on track variance.

2. COMPONENT CHARACTERIZATION

2.1 Beam-Steering Stages

Fine angle beam-steering can be accomplished using angular or linear position transducers, and both are amenable to miniaturization for spacecraft applications. As a baseline, we tested a commercially available macro-scale tip/tilt mirror, which was designed for very fine pointing and stabilization (~ 1 μrad) in two axes. A comparable commercially available macro-scale position transducer was tested in order to evaluate an inline beam-steering architecture utilizing a

matched pair lens set. A custom meso-scale position transducer, developed by NIST, was also tested. This stage is extremely compact, provides maximum axial directivity, and can be redesigned for various mechanical gains and actuator ranges. Each beam-steering mechanism is structurally unique, however each is piezoelectrically actuated by a signal between 0 V and 100 V. Therefore, each stage exhibits an inherent hysteresis, which is an important consideration for optimal controller design.

The measured 'plant' responses (incorporating each stage) include the responses of the high voltage amplifier, the beam-steering device and mount, the quadrant photodetector, and the divider circuit, which calculates position error from the quadrant sum and difference signals, as shown in Figure 2.

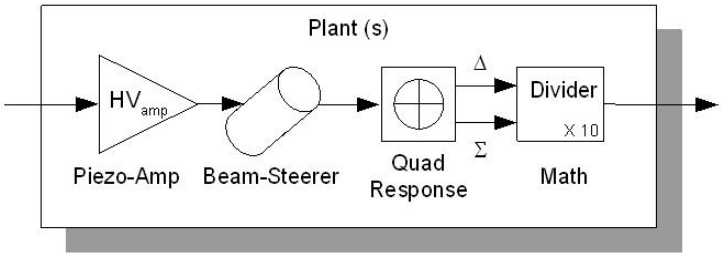

Figure 2: Plant block diagram, consisting of the actuator driver amplifier, beam-steering actuator, quad cell response (including implicitly any optical angular gain), and subsequent monopulse arithmetic.

The three beam-steering devices that we tested and compared for our applications are pictured in Figure 3.

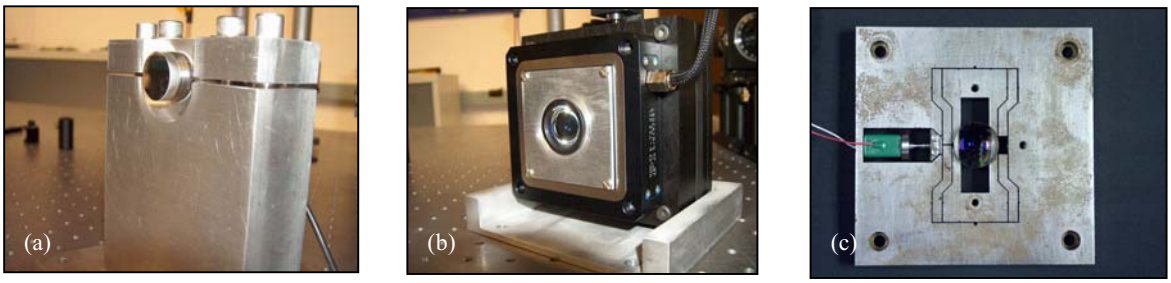

Figure 3: (a) Commercial (Polytec PI) two-axis tip/tilt mirror and actuator mounted to a fixture used to suppress any unwanted vibration modes, (b) commercial (Polytec PI) linear transducer mounted with one fast lens attached to the moving frame (while the other lens is fixed to the mounting structure), and (c) a plan-view picture of the NIST transducer with small lens attached to the inner stage.

The fast-steering mirror shown in Figure 3(a) is an 'ultra-fast' piezo-driven tip/tilt stage with a 25.4 mm diameter glass mirror surface. The device is operated open-loop, containing no internal sensor or feedback mechanism to mitigate hysteresis. Its manufacturer-specified angular range is ±2.5 mrad with a 0.05 μrad resolution, which is limited by the noise of the drive amplifier. Its resonant frequency is in the range of 3kHz. Its plant (magnitude and phase) response is shown in Figure 4(a) for both axes. The commercial linear transducer shown in Figure 3(b) is a piezo-driven x-y nano-positioner with a 25.4 mm diameter, 25.4 mm focal length singlet lens mounted to the 50 mm x 50 mm clear aperture of the stage. By positioning a matching lens at twice the focal length of the nano-positioner lens, fine-angle beam-steering with unity angular gain is achieved. The device was also operated open-loop for our tests, without using its internal feedback sensors. The manufacturer-specified travel range is ±50 μm with a 0.5 nm resolution. Operating the beam-steerer with lens focal lengths of 25.4 mm, these displacements translate to an angular range of ±2 mrad and angular resolution of 0.02 μrad. The resonant frequency of the stage is in the range of 500 Hz, including a mechanical load of ~40 g. Its plant response is shown in Figure 4(b) for both axes.

A novel class of nano-positioning mechanisms has previously been developed, as discussed by Dagalakis et al.[4], which may be particularly useful in the development of high-bandwidth, high-accuracy beam-steering devices. These nano-positioners utilize a parallel cantilever design, which has been shown to significantly reduce off-axis parasitic

positioning errors that are typical in other flexure mechanism design approaches. Furthermore, the design can be easily optimized for the required motion amplification of the piezoelectric actuator, as well as the desired stiffness and primary natural frequency. This design has been adapted to create the nano-positioner shown in Figure 3(c), which has been scaled down by a factor of four compared to the mechanism previously studied [4]. The overall size of the stage is 6.36 cm x 6.36 cm, where the actual nano-positioner is only 4.6 cm x 4.6 cm. Note the position of the 12.5 mm diameter lens is confined to the inner (moving portion) of the stage. The flexure mechanism is driven by a piezoelectric actuator connected to it through a coupler. This coupler is a spherical flexure that is used to minimize the moment placed on the actuator due to axis alignment issues. The actuator has a range of 0 μm to 9.1 μm for an applied voltage range of 0 V to 150 V, resulting in a displacement range of 0 μm to 91 μm due to a motion amplification gain of ten in the flexure mechanism. Similar to the commercially available x-y nano-positioner discussed in the previous section, this nano-positioner can be utilized as a beam-steerer by scanning a lens within the path of the beam. However, the mechanism has not been specifically designed for this purpose, and the prototype only has a single degree of freedom. Therefore, the results presented in this paper will be used in future work to adapt the mechanism design for this particular application.

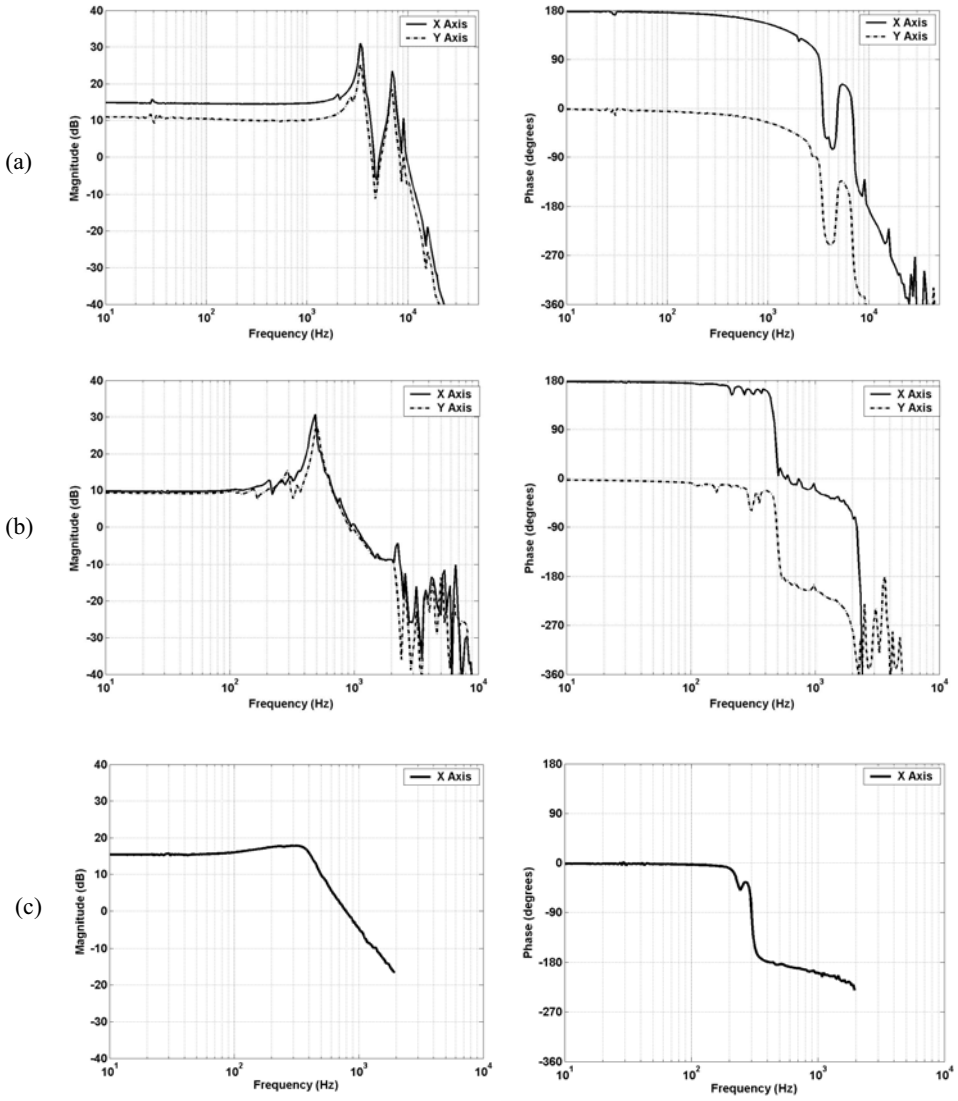

Figure 4: (a) Tip/tilt mirror plant response for magnitude (left plot) and phase (right plot) in both the x and y-axes; (b) Commercial linear position transducer plant response for magnitude (left) and phase (right) in both the x and y-axes; and (c) NIST linear position transducer plant response (x-axis applies only) for magnitude (left) and phase (right).

In this study, a voltage range of 0 V to 100 V is used, resulting in a travel range of ±30 μm with an anticipated resolution of 0.3 nm, based on amplifier noise and data acquisition characteristics. Operating the beam-steerer with lens diameters of 12.5 mm and focal lengths of 15 mm, these displacements translate to an angular range of ±2 mrad and angular resolution of 0.02 μrad. The resonant frequency of the stage is in the range of 300 Hz including a mechanical load of ~1 g. Its plant (magnitude and phase) response is shown in Figure 4(c) for just the x-axis. The specifications on the various performance parameters are summarized in Table 1.

Table 1: Beam-Steering Technologies

Beam-Steering Stage	Travel Range	Travel Resolution	Focal Length*	Angular Range	Angular Resolution	Resonant Frequency
Polytec PI Macro Tip/Tilt Mirror	--	--	--	±2.5 mrad	0.05 μrad	~3 kHz
Polytec PI Nano-Positioner	±50 μm	0.5 nm	0.0254 m	±2 mrad	0.02 μrad	~500 Hz
NIST Nano-Positioner	±30 μm	0.3 nm	0.015 m	±2 mrad	0.02 μrad	~300 Hz

* Focal length is selectable and yields angular range and resolution accordingly.

2.2 Tracking Sensor

The principal tracking sensor used in this effort was a quadrant photodiode detector shown in Figure 5. It utilizes post-detection monopulse arithmetic to form the error signals. Quad cell electrical output versus lateral laser spot position can be converted to the output versus angle of the received beam for a given receiver lens focal length by the relation: $\Delta\theta = \Delta x/f$, for sufficiently small angles ($\leq$ 0.1 radians). Beam displacement is calculated along the x- and y-axes of the detector and then removed in the system control loop for detector beam-centering and tracking. In general, the laser spot can appear on the detector active area as suggested in Figure 5, i.e., a Gaussian beam with an arbitrarily oriented elliptical cross-section.

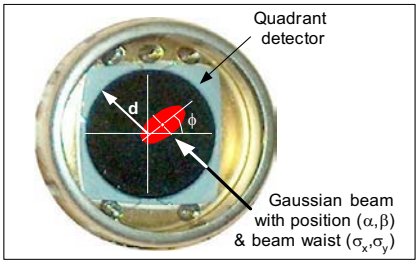

Figure 5: Actual quad cell photodiode, with geometric parameters used for calculating its response to an elliptical Gaussian beam.

Tip/tilt errors are calculated by first specifying the beam power, i.e., the detector current, times the responsivity of each quadrant on the A, B, C and D channels of the detector. These "powers" are added and subtracted in the following manner to calculate these so-called monopulse errors:

$$\varepsilon_{tilt} = \frac{(A+D)-(B+C)}{\Sigma} \qquad \varepsilon_{tip} = \frac{(A+B)-(C+D)}{\Sigma} \tag{1}$$

where $\Sigma = A + B + C + D$. Since the beam on the photo-detector is typically Gaussian in shape, the values for A, B, C, and D in equation (1) can be calculated as the "volume" of the Gaussian falling on the A, B, C, and D detector channels, respectively.

For a beam displacement of α on the x-axis and β on the y-axis, a local beam tilt of ϕ, (untilted) beam variances of σ_x and σ_y, and detector radius d, the (normalized) volume integral for a Gaussian beam is:

$$I = \int\int e^{-\left[\frac{(x-\alpha')^2}{2\sigma_x^2}+\frac{(y-\beta')^2}{2\sigma_y^2}\right]} dxdy \Rightarrow \int_{\theta_1}^{\theta_2}\int_{0}^{d} e^{-\left[\frac{(r\cos\theta-\alpha')^2}{2\sigma_x^2}+\frac{(r\sin\theta-\beta')^2}{2\sigma_y^2}\right]} rdrd\theta\,, \tag{2}$$

where there is a simple rotation coordinate transformation between [α',β'] and [α,β] by the angle ϕ, which accounts for the orientation angle of the laser beam major axis with respect to the quad-cell coordinate system. Equation (2) can then be simplified to**:**

$$I = \frac{e^{-\xi}}{2\gamma}\int_{\theta_1}^{\theta_2}\left[1 - e^{-\gamma d^2+\eta d} + (\eta/2)\sqrt{\pi/\gamma}\,(e^{\eta^2/4\gamma})\left[erf\left(\sqrt{\gamma}\,(d-\eta/2\gamma)\right) - erf\left(\sqrt{\gamma}\,(-\eta/2\gamma)\right)\right]\right]d\theta \tag{3}$$

where: $$\gamma = \frac{\cos^2\theta}{2\sigma_x^2} + \frac{\sin^2\theta}{2\sigma_y^2}\,, \qquad \eta = \frac{\alpha'\cos\theta}{\sigma_x^2} + \frac{\beta'\sin\theta}{\sigma_y^2}\,, \text{ and} \qquad \xi = \frac{\alpha'^2}{2\sigma_x^2} + \frac{\beta'^2}{2\sigma_y^2} \tag{4}$$

The normalized signal levels from each quadrant: A, B, C, and D, result from evaluating equation (3) over different angle limits ($\theta_1 \rightarrow \theta_2$) as defined by: [−ϕ, π/2 − ϕ] for A, [π/2 − ϕ, π − ϕ] for B, [π − ϕ, 3π/2 − ϕ] for C, and [3π/2 − ϕ, 2π − ϕ] for D. In the model plots shown below ϕ is set to zero, and one variable (y) is set to zero. This yields the error curves versus beam displacement along the x (or y)-axis shown in Figures 6(a) and (b) for a circular Gaussian intensity beam with 500 nW total beam power (P) and 1 mm, 2.5 mm, and 5 mm standard deviations ($\sigma_x = \sigma_y = \sigma$). Detector radius (d) is 5 mm and responsivity (S) is 0.6 A/W. Two levels of DC noise current were added.

To scale the normalized integral of equations (2) and (3), the total beam power is equated with the total distribution, and the H_0 for the σ of interest is computed:

$$P = 500nW = \frac{H_0}{2\pi\sigma^2}\int_0^{2\pi}\int_0^{\infty} e^{-\frac{r^2}{2\sigma^2}} rdrd\theta \tag{5}$$

The output current for each channel is calculated by multiplying the integral of equation (3) by the scaling factor in equation (5), multiplying by the responsivity, and adding the noise current. This particular quad cell model includes only channel gain, bias errors, additive white Gaussian channel noise, and, of course, the monopulse arithmetic. For sufficiently low signal-to-noise ratios we would also incorporate A/D quantization noise as well as any digital filter round-off or truncation errors in a discrete implementation.

For the model described above the transfer characteristics are shown in Figures 6(a) and (b) for three different laser spot sizes (in mm), showing a saturation effect due to the finite beam size, which determines the tradeoff between angle dynamic range and null position sensitivity. As a result, we set the spot size to approximately half the quad cell diameter. We then measured the quad cell response as part of our calibration and sensor angular sensitivity measurement, which is shown in Figure 6(c).

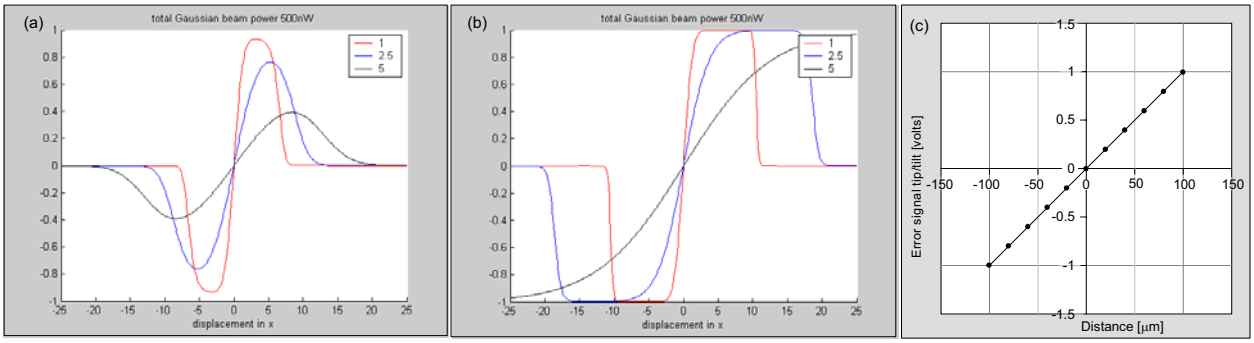

Figure 6: Tilt errors for Gaussian beam with (a) 5 nA and (b) ~zero DC noise current, and (c) measured data fitted with a linear model. The fit was virtually identical in both axes and given by ε = 0.01x with correlation coefficient = 1.

3. SYSTEM ARCHITECTURE AND CONTROLLER IMPLEMENTATION

3.1 Tracking System Architecture

The physical architecture of the tip/tilt tracking loop consists of a DC source laser incident on the tip/tilt mirror at 45º. Additional mirrors are used at 45º angles to bend the light path and extend the moment arm of the beam in order to match the angular range of the tip/tilt actuator to the angular extent of the quadrant photodetector. The beam at this distance (in the range of ~1 m) is divergent enough to create a spot size appropriate for the size of the detector (~0.7 cm). For the test of a position transducer beam-steerer, the actuator containing the dynamic lens is mounted between two of the mirrors used to fold the light path to the quad. The stationary lens is positioned further along in the beam path at twice its focal length from the dynamic lens. The quadrant photodiode-measured position error signals are conditioned appropriately (i.e., scaled and offset) and fed to the analog-to-digital converters (ADCs) of the DSP controller. The actuator control signals from the digital-to-analog converters (DACs) of the DSP controller are fed back through a conditioning circuit to the Polytec PI high voltage amplifier, which directly drives the piezoelectric devices. A block diagram of the tracking system is shown in Figure 7. Figure 8 shows the optical layout of the tracking test bed.

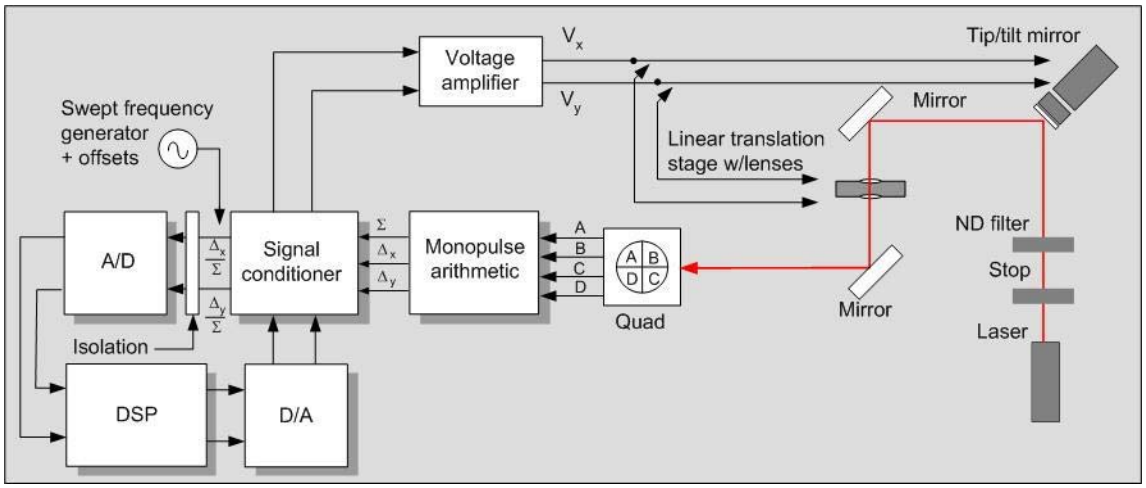

Figure 7: Beam-steering and quadrant photodiode tracking system architecture.

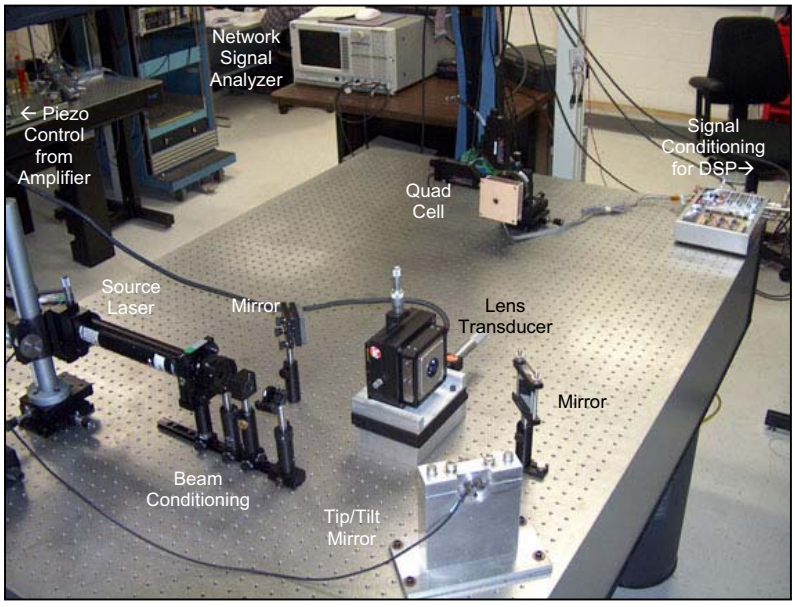

Figure 8: Beam-steering and tracking test bed optical layout.

3.2 Digital Controller and Algorithm

Initial work with the controller was done using an analog circuit, developed at APL, in order to gain experience with the beam-steerers and tracking detectors to be tested. Tracking performance was achieved, but once the equipment was acquired and integrated, the transition was quickly made to a digital system, as it was an important focus of our effort.

A digital signal processor-based board developed by LYR Signal Processing (the LSP SignalMaster) was used as the controller platform for the pointing and tracking system. The choice of the controller was based on two criteria: flexibility and ease of implementation and programming. LYR Signal Processing cards support both needs by having a library of pre-programmed functions and block-sets in MATLAB Simulink. In addition, block-sets were available to control the on-board ADCs and DACs, which enable a more versatile interface for a variety of control and sensor implementations.

Our design approach leveraged previously developed and on-going modeling efforts in Simulink to be converted to DSP blocksets and run directly on the DSP boards. This allowed the modeling and simulation work to flow quickly into the DSP hardware implementation, saving both cost and time. Table 2 gives an overview of the digital controller hardware used. Figure 7 shows the location of the DSP system in the control system architecture. The overall function of the DSP system was to sample the error produced by the quadrant detectors and provide an appropriate voltage to the actuator to null out the error.

Table 2: Digital Controller Description

Digital Control System Parameters	
Manufacturer	LYR Signal Processing Signal Master cPCI Card
Sampling Rate	48 kHz
DSP Processor	TMS320C6701 Floating Point
A/D Converter	2-CS4228 Codec 24 Bit ΣΔ
D/A Converter	2-CS4228 Codec 24 Bit ΣΔ
Programming	Code Composer Studio with Simulink Block-sets

A Proportional Integral (PI) controller algorithm was used to control the various beam-steering actuators. Although this would not necessarily achieve optimum performance, it would enable us to compare them on an equal basis. PI controllers are extremely common in industrial and commercial controllers and were considered for this application because of their robustness, versatility, and ease of design. Equation (6) shows the set of transfer function equations used for a digital implementation of the PI controller. K_p is the proportional gain constant, K_i is the integral constant, and T is the sampling time. The proportional gain K_p is used to increase the step response of the control loop. As a result of judiciously designing the proportional term, the output follows the input faster. The controller also has an integral term, which is used to decrease the steady state error of the control loop. Used in tandem, the proportional and integral terms provide for a robust control algorithm.

$$G_c(z) = \frac{B_1 z + B_2}{z - 1}; \quad B_1 = K_p + K_i T; \quad B_2 = -K_p; \tag{6}$$

Tuning of the PI controller was done using the Zeigler-Nichols method and then optimized for integral gain. This method is readily used for complex systems, as it does not require an accurate plant model to be effective.[6]

MATLAB Simulink was used to design the controller for each of the beam-steerers tested. Digital filters were used to inhibit response of the beam-steering stages at and above their resonant frequencies. Besides the custom blocksets from Lyrtech LSP that were used to control the ADC and DAC interfaces, typical Simulink blocks were used to implement the digital integrator, differentiator, and filter functions. A representative controller model is shown in Figure 9.

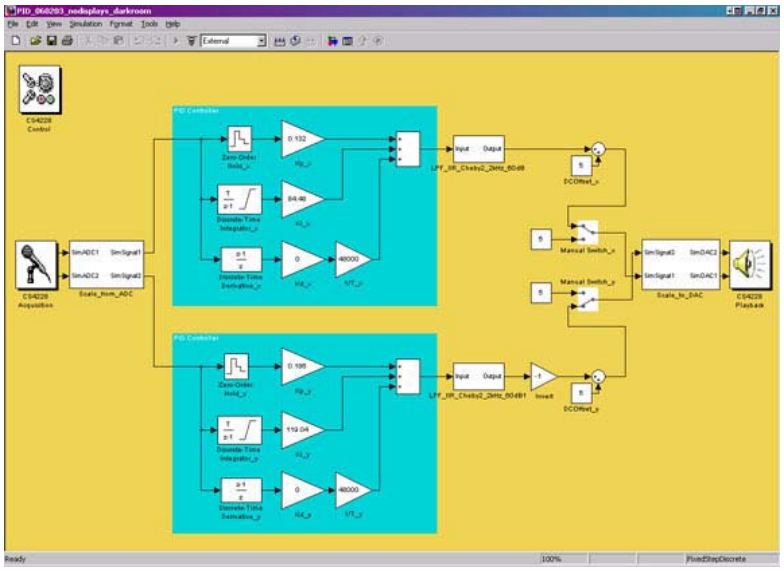

Figure 9: DSP implementation of PI controller using MATLAB Simulink.

4. TRACKING PERFORMANCE

4.1 Measurement Procedure

The tracking response of each beam-steerer was measured for various incident optical power levels. The control loop was designed for each beam-steerer axis independently, although each used the same PI controller structure. An open-loop and closed-loop response was determined for each axis of the device, with the x- and y-axes corresponding to the horizontal and vertical directions respectively. A Stanford Research Systems network signal analyzer was used to inject an error signal directly into the interface scaling circuitry for the axis under test. The transfer function between the quadrant detector error and the injected signal was observed for closed-loop response. The transfer function between the quadrant detector error and the input to the digital controller was observed for open-loop response. An external monitor of the quad error was also used to track the angular statistics of the beam-steerer during track based on the quadrant error vs. displacement calibration and the distance between actuator and detector. The standard deviation of the quadrant error was observed for various incident optical power levels.

A more meaningful measure of performance for spacecraft operation, however, is not the open-loop or closed-loop response, but the rejection response of the control system. The rejection response describes the capability of the control loop to track-out disturbances caused by the spacecraft vibrational modes. Rejection, $F_R(s)$, can be predicted through the calculation of equation (7):

$$F_R(s) = 1 - F_C(s) = \frac{1}{1 - F_O(s)} \tag{7}$$

where $F_c(s)$ and $F_o(s)$ are the closed-loop and open-loop responses of the tracking loop respectively. Rejection performance was calculated for each axis of each beam-steerer and is plotted along with the open-loop and closed-loop responses in the next section.

4.2 Performance Comparisons

Open- and closed-loop responses were measured and used to predict rejection ratios, which are all displayed in Figures 10-14. A comparison of the performance of the three beam-steerers is summarized in Figure 15. In addition, the standard deviation of each transducer was determined from the collected tracking statistics, ignoring the occasional interference signal. These data are summarized in Figure 16.

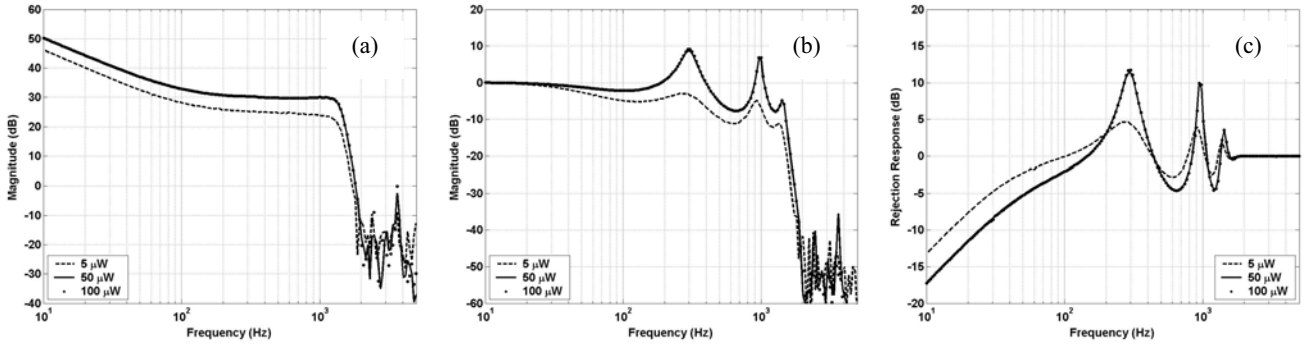

Figure 10: Tip/tilt mirror x-axis response (a) open-loop and (b) closed-loop measurements, (c) rejection prediction.

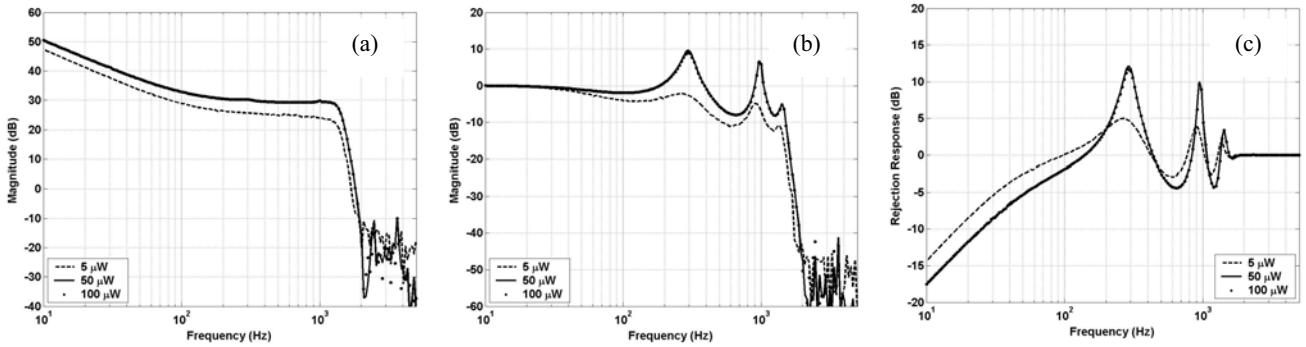

Figure 11: Tip/tilt mirror y-axis response (a) open-loop and (b) closed-loop measurements, (c) rejection prediction.

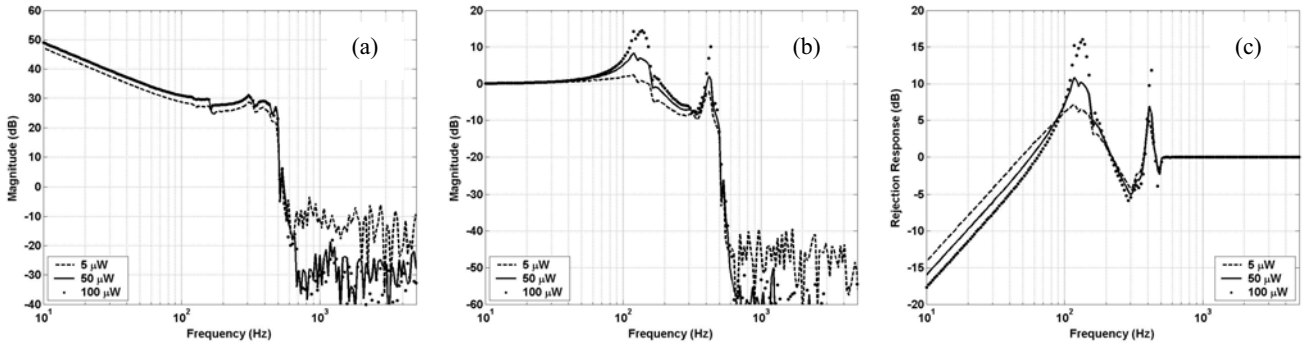

Figure 12: Commercial lens transducer x-axis response (a) open-loop and (b) closed-loop measurements, (c) rejection prediction.

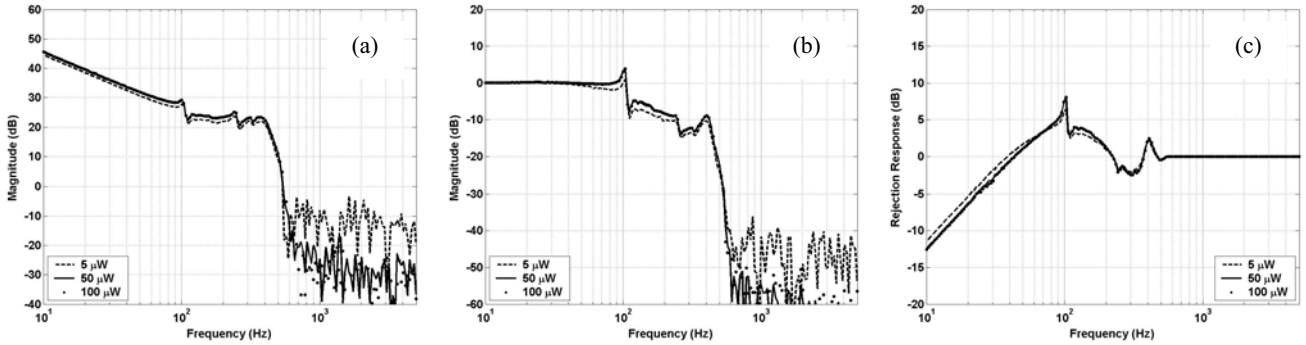

Figure 13: Commercial lens transducer y-axis response (a) open-loop and (b) closed-loop measurements, (c) rejection prediction.

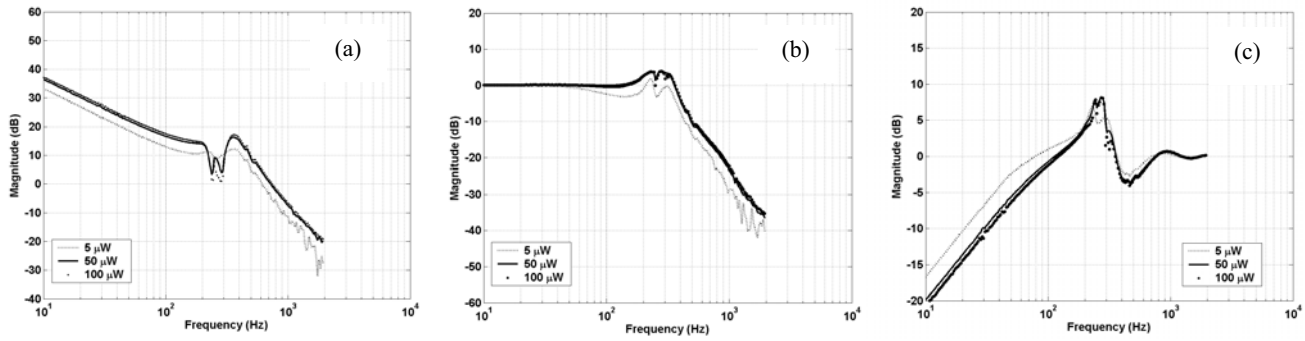

Figure 14: NIST lens transducer x-axis response (a) open-loop and (b) closed-loop measurements, (c) rejection prediction.

A plot of the standard deviation of the beam-steerers in Figure 16 suggests that for these measurements we are operating at the limit of the quad cell, i.e., just above its noise floor, which is thus just sufficient to establish a lower bound on overall system tracking accuracy, albeit under no external excitation. Thus, by knowing the upper bound or the beam-steerer angular range, we can determine an approximate angular dynamic range. For the tip/tilt device we obtain 33 dB, assuming its upper bound is ±2.5 mrad. For the commercial linear transducer, it is 38 dB, assuming its linear range is ±50 μm. For the NIST transducer it is 31 dB, assuming its linear range is ±30 μm. Of course, for each of the lens transducers, the maximum angular range and minimum angular resolution are dependent on the focal length of the selected lens. However, angular dynamic range is independent of the lens focal length.

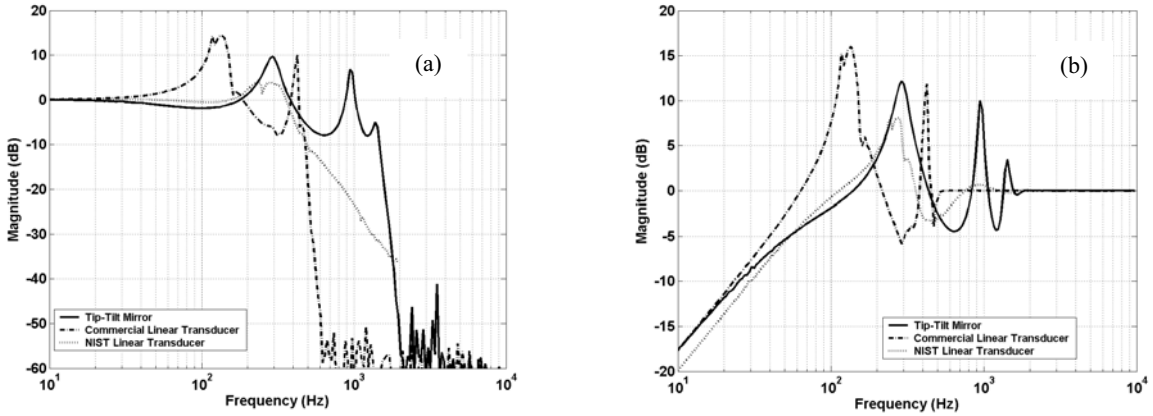

Figure 15: Comparison of beam-steerer x-axis responses (a) closed-loop, (b) rejection prediction.

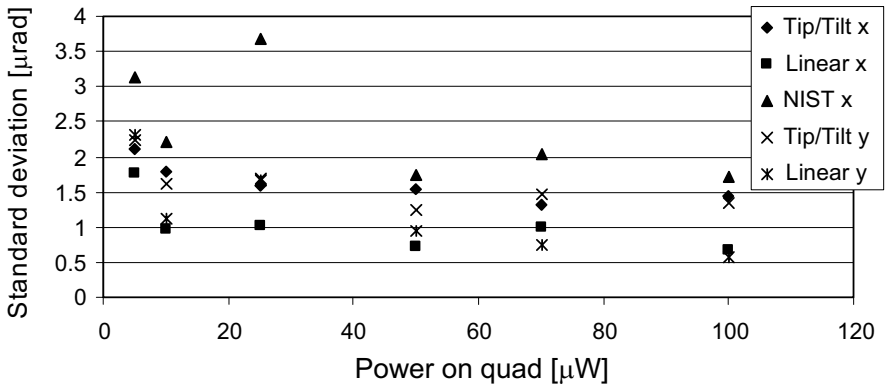

Figure 16: Standard deviation of track noise vs. incident power on quad cell for each technology and the appropriate axes.

5. CONCLUSIONS AND FUTURE WORK

The presented results have shown that the NIST linear transducer performs better than the tested commercial linear transducer but not as well as the tip-tilt mirror, with respect to closed-loop bandwidth and disturbance rejection. However, the tracking error was somewhat larger for the NIST linear transducer compared to the other devices. This may be due to the fact that it is a single axis mechanism which cannot compensate for errors along the orthogonal axis of the photo detector. This will be corrected in the next generation mechanism which will have motion along both x and y axes. Due to these results, and the fact that the nano-positioner is significantly smaller in size and mass compared to the other devices, we believe that this technology can play a role in future optical communication systems. This will require a design modification to improve bandwidth and tracking error performance. This can be achieved by reducing the mass of the mechanism by removing non-structural material from the design. In addition, the stiffness can be increased by optimizing the flexure thickness for the chosen material. The use of other materials will also be explored, such as beryllium copper, to improve the stiffness to mass ratio based on the desired travel range of the mechanism. Finally, it is believed that electrical considerations contributed to the tracking error in the NIST linear transducer. The voltage amplifier which was used in the experiments was designed specifically for the other mechanisms used in the tests. Therefore, an amplifier tuned specifically for the piezoelectric actuator used in the NIST linear transducer will be used in future experiments to evaluate the effect. With these modifications among others, a significant improvement in the reported bandwidth and tracking error performance is expected, while maintaining the size and mass advantages.

In the future, several improvements will also be made to the tracking sensor, including band-limiting electrical and spectral filters and internal gain, or we will transition to a focal plane array. Furthermore, we will improve the controller design by using a signal interface with much less acquisition latency, which was a significant source of bandwidth limitation in our tracking system. Ultimately, we will specify and build a robust field programmable gate array (FPGA) implementation of the digital tracking controller. Our goal is to achieve the desired rejection ratio for disturbances up to at least 100 Hz, reduce our track variance to ~ 500 nrad, and achieve a dynamic range of more than 40 dB with a peak-to-peak angular range of at least 10 mrad. This will enable us to capture a typical spacecraft attitude control system capability while stabilizing to less than 1 μrad.

ACKNOWLEDGEMENTS

The authors would like to acknowledge the valuable contributions of D.T. Winters, J.R. Jensen, and J. Hernandez to this paper.

DISCLAIMER

Commercial equipment and materials are identified in order to adequately specify certain procedures. In no case does such identification imply recommendation or endorsement by the Johns Hopkins University Applied Physics Laboratory or the National Institute of Standards and Technology, nor does it imply that the materials or equipment identified are necessarily the best available for the purpose.

REFERENCES

1. "Optical and microwave communications system conceptual design for a realistic interstellar explorer," with R.S. Bokulic, G.B. Andrews, R.L. McNutt, Jr., and N. Dagalakis, Proceedings SPIE Vol. 4821, Free-Space Laser Communications and Laser Imaging II, 9-11 July 2002 Seattle, WA, pp. 225-236.
2. Private communication, T. E. Strikwerda, JHU/APL Space Department, 25 March 2002.
3. "Conceptual design and algorithm evaluation for a very accurate imaging star tracker for deep-space optical communications," with D.E. Maurer, SPIE Vol. 4821, Free-Space Laser Communications and Laser Imaging II, 9-11 July 2002 Seattle, WA, pp. 237-247.
4. N. G. Dagalakis, J. A. Kramar, E. Amatucci, & R. Bunch, "Kinematic modeling and analysis of a planar micro-positioner", *Proceedings of the ASPE Annual Meeting*, Crystal City, VA, pp. 135-138, 2001.
5. "Development of a laser transceiver system for deep-space optical communications," with J.R. Bruzzi, W.P. Millard, J.R. Connelly, and J. Liu, SPIE Vol. 4821, Free-Space Laser Communications and Laser Imaging II, 9-11 July 2002 Seattle, WA, pp. 202-213.
6. F. Nekoogar and G. Moriarty, Digital Control using Digital Signal Processing, Prentice Hall, Upper Saddle River, NJ, 1998.